Research Article | Open Access

Soft Science

Luo *et al. Soft Sci.* **2026**, *6*, 57 **DOI:**10.20517/ss.2026.49

Electromagnetic synergistic optimization of conductive NiCo-MOF with excellent electromagnetic wave absorption properties

Kaiyan Luo[1], Yupeng Hu[1], Teng Zhou[1], Xiaonan Liu[2,*], Maoxia Lu[1], Zhi Lei[1], Daohai Zhang[1,*], Wei Gong[1,*]

Keywords:
Electromagnetic wave absorption, HHTP, dielectric loss, magnetic loss, dielectric-magnetic loss synergistic effect

Citation: Luo, K.; Hu, Y.; Zhou, T.; Liu, X.; Lu, M.; Lei, Z.; Zhang, D.; Gong, W. Electromagnetic synergistic optimization of conductive NiCo-MOF with excellent electromagnetic wave absorption properties. *Soft Sci.* **2026**, *6*, 57. https://dx.doi.org/10.20517/ss.2026.49

Received: 8 Mar 2026
First Decision: 26 Mar 2026
Revised: 3 Apr 2026
Accepted: 23 Apr 2026
Published: 3 Jul 2026

Academic Editor:
Guanglei Wu
Copy Editor:
Xing-Yue Zhang
Production Editor:
Xing-Yue Zhang

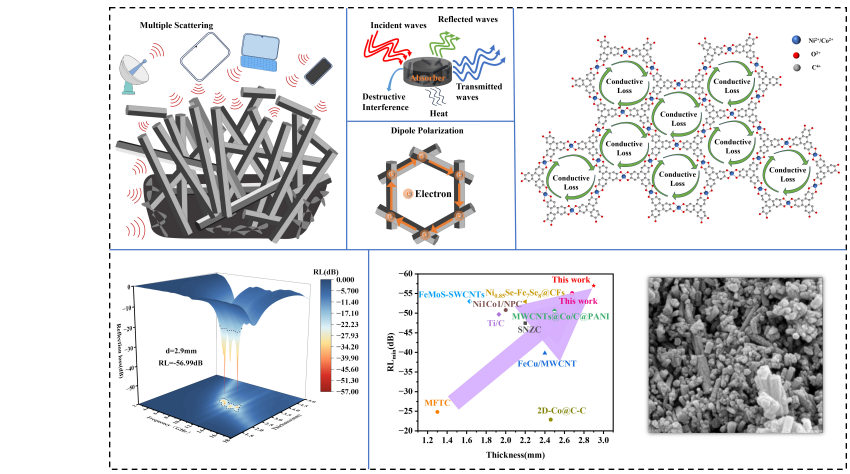

Abstract

The rapid development of information technology has given rise to an urgent demand for high-efficiency electromagnetic wave absorbing materials. It is a challenge for wave-absorbing materials that address the electro-magnetic synergistic effect to develop high-efficiency electromagnetic wave (EMW) materials that can not only reduce the electromagnetic interference generated by electronic devices in daily use but also exhibit a certain degree of stealth in the military field. To study and prepare high-efficiency EMW materials, this paper uses the solvothermal method to prepare NiCo-HHTP, and systematically investigates their electromagnetic wave absorption performance and absorption mechanism. The research shows that the composite material NCH1 obtained in this experiment achieves a minimum reflection loss (RL_{min}) value of -56.99 dB and an effective absorption bandwidth of 6.51 GHz at a relatively thin matching thickness of 2.9 mm. The polarization effect endows it with good conductive loss, and the magnetic central metal gives it a certain degree of magnetic loss. The synergistic effect of dielectric loss and magnetic loss makes the material exhibit a good wave-absorbing effect. This simple and efficient preparation method provides a new strategy for the preparation and application of metal-organic framework materials in EMW absorption.

[1]School of Chemical Engineering of Guizhou Minzu University, Guiyang 550025, Guizhou, China.
[2]National Engineering Research Center for Compounding and Modification of Polymer Materials, Guiyang 550014, Guizhou, China.

***Correspondence to:** Prof. Daohai Zhang, Prof. Wei Gong, School of Chemical Engineering of Guizhou Minzu University, Guiyang 550025, Guizhou, China. E-mail: zhangdaohai6235@163.com; gongw@gznu.edu.cn; Prof. Xiaonan Liu, National Engineering Research Center for Compounding and Modification of Polymer Materials, Guiyang 550014, Guizhou, China. E-mail: liuxiaonan309@163.com

INTRODUCTION

With the advancement of the information age, electronic devices and information technology have experienced rapid development, leading to an increasing prevalence of electromagnetic (EM) pollution issues[1-3]. On the one hand, electromagnetic waves (EMW) are steadily eroding human health and posing a potential threat to the safety of our living environment[4-6], The harm of EMW to the human body primarily depends on its frequency and intensity[2]. On the other hand, in the military domain, electromagnetic interference can disrupt the normal operation of radar systems and communication equipment[7]. Traditional electromagnetic wave absorbers include magnetic materials such as ferrites[8] and magnetic metals[9], carbon-based materials like graphene[10] and carbon nanotubes[11], ceramics[12], as well as conductive polymers and their composites. However, their application scope is limited by shortcomings such as restricted absorption bandwidth, weak energy dissipation, and difficulty in precise tuning[13].

MOFs and their derivatives have the advantages of high specific surface area, porous structure, and precise controllability of components and morphology, making them a core research direction for lightweight, broadband, and high-loss wave-absorbing materials. Geng *et al.*[14] reported the introduction of ZIF-67 nanoparticles into a polysilazane precursor via a physical mixing method, followed by high-temperature pyrolysis to synthesise silicon-containing polymer-derived Si-C-N ceramics (Co-SiCN). The results indicate that the incorporation of ZIF-67 promotes the formation of dielectric loss phases such as SiC nanocrystals, CoSi nanocrystals, and free carbon, resulting in a maximum effective absorption bandwidth of 3.0 GHz at an ultra-low thickness of 1.05 mm, with a minimum reflection loss of -46.4 dB at a low frequency of 6 GHz. Xu and colleagues[15] reported a polymer-based EVA-Fe_3O_4-GO (EFG) aerogel, prepared using a direct heating cross-linking process and pore modulation engineering. The synergistic combination of Fe_3O_4 nanoparticles and GO sheets enhanced the magnetic medium loss, while the porous structure promoted multiple microwave scattering. The material exhibited a minimum reflection loss (RL_{min}) of -34.3 dB at 2.0 mm and an effective absorption bandwidth (EAB) of 4.56 GHz in the high-frequency range. Ma *et al.*[16] introduced heteroatoms (N and S) co-doped graphene (N, through the co-doping of nitrogen and sulfur, graphene is endowed with abundant defects and disordered sites, which effectively enhances interfacial polarization and dipole polarization, that is, effectively enhances the dielectric loss of the material. The RL_{min} of the composite material reaches -47.7 dB at EAB 4.24 GHz. This demonstrates the broad range of applications of MOF in the field of wave-absorbing materials.

Conductive metal-organic frameworks (cMOFs) possess the characteristics of MOFs, including a high surface area, a porous structure, high density of active sites, and adjustable formulation. In addition, due to their unique π-π conjugated structure, they exhibit excellent electrical conductivity and adjustable central metals (which can adjust the magnetic loss constant to achieve the effect of electrical-magnetic balance)[17,18]. These characteristics suggest that cMOFs have broad application prospects in the field of electromagnetic wave absorbing materials. In recent years, a series of representative monometallic MOFs research systems have been extensively studied. For example, Shan *et al.*[19] (2022) systematically investigated their electromagnetic wave absorption performance and absorption mechanisms by constructing monometallic M3(HHTP)2 MOFs of Cu, Zn and Ni; Zhang *et al.*[20] (2023) synthesized rod-shaped conductive MOFs (cMOFs) composed of tunable metal ions such as Zn, Cu, Co or Ni and hexahydroxytriphenylene (HHTP) ligands to obtain adjustable dielectric properties and thereby realize electromagnetic wave absorption. Although these single-metal MOFs have laid a foundation for material design, a single component cannot simultaneously meet the comprehensive requirements of strong absorption, broadband performance and light weight. To balance the attenuation effects of dielectric loss and magnetic loss, the bimetallic modulation

strategy is widely applied in the research and development of metal-organic framework microwave absorbing materials. For example, Chen *et al.*[21] constructed a series of pristine MOFs with precise and controllable electrical conductivity through a doping and alloying strategy, and synthesized the bimetallic $Cu_{1.3}Ni_{1.7}(HITP)_2$. The controllability is attributed to the changes in free carrier concentration and subtle differences in interlayer displacement or spacing, both of which originate from the atomic tuning of heterogeneous metals. Zhang *et al.*[22] synthesized bimetallic NiCu-HHTP cMOFs with precisely controllable interlayer spacing. The coexisting structure of nickel ions and copper ions can fine-tune charge transport, electronic band structure and dielectric properties. Therefore, the bimetallic HHTP structure can achieve stronger electromagnetic wave attenuation capability and a wider effective absorption bandwidth, providing a feasible design strategy for the research and development of high-performance conductive metal-organic framework electromagnetic wave absorbing materials.

In this paper, NiCo-HHTP was prepared by the solvothermal method using HHTP as the ligand. Conductive MOFs have received little attention from researchers in the domain of electromagnetic wave absorption. Starting from the composition and morphology, HHTP is selected as the ligand. By changing the proportion of the central metal, the morphology and structure of the material are regulated, and the magnetic loss constant is changed to form a dielectric loss and magnetic loss. The complementary/synergistic effect of loss has been demonstrated to optimise the impedance matching of the material, thereby ensuring the material achieves a satisfactory electromagnetic synergistic effect[19]. The composite material NCH1 prepared in this experiment achieved a RL_{min} value of -56.99 dB and an EAB of 6.51 GHz at a matching thickness of 2.9 mm. cMOFs materials can simultaneously achieve the synergistic effect of multiple loss mechanisms such as conduction loss, dielectric loss, magnetic loss, and interfacial polarization. In-depth study of its electromagnetic response laws helps to reveal the contributions of heterogeneous interfaces, defects, and dielectric losses to electromagnetic wave attenuation, and provides theoretical support for the mechanism research of a new generation of high-performance wave-absorbing materials.

EXPERIMENTAL

Experimental materials and preparation methods

The chemical reagents used in this study, including hexahydroxytriphenylene (HHTP), cobalt(II) acetate tetrahydrate [$Co(CH_3COO)_2{\cdot}4H_2O$], nickel(II) acetate tetrahydrate [$Ni(CH_3COO)_2{\cdot}4H_2O$], isopropanol (IPA), and anhydrous ethanol, were all purchased from Aladdin Reagent Co., Ltd. (Aladdin, Shanghai, China). The chemicals utilised in this study were all commercially available and employed without further purification.

Preparation method of M-HHTP (M = Ni, Co)

Dissolve 0.5 mmol of HHTP in 12 mL of isopropanol, then centrifuge and stir at 80 revolutions per minute at room temperature for 20 min. Dissolve 0.7 mmol of acetate in 15 mL of deionized water and stir at 60 revolutions per minute for 10 min at room temperature. Then slowly add the acetate aqueous solution to the isopropanol dispersion containing HHTP and stir at 80 revolutions per minute at room temperature for 20 min to ensure thorough mixing of the two solutions. Subsequently, react in a reactor at 80 °C for 20 h. Subsequent to cooling to ambient temperature, collection of the precipitate by centrifugation should be undertaken, along with thorough washing with deionised water and ethanol. The final stage of the process is to dry the product in a vacuum oven at 60 °C for 15 h, which will result in the target product being obtained.

Under a fixed ligand HHTP concentration of 0.5 mmol, five M-HHTPs were synthesised by altering the acetate ratio: when Ni^{2+}:Co^{2+} = 1:0, it was designated as NH; when Ni^{2+}:Co^{2+} = 0:1, as CH; when Ni^{2+}:Co^{2+} = 1:3, as NCH1; when Ni^{2+}:Co^{2+} = 3:1, as NCH2; and when Ni^{2+}:Co^{2+} = 1:1, as NCH3.

Characterisation

The microscopic morphology and elemental distribution of the samples were observed by scanning electron microscopy (SEM) combined with energy-dispersive X-ray spectroscopy (EDX). Powder X-ray diffraction (PXRD) was used to analyze the crystal structure and chemical bonding characteristics of the as-prepared materials.

X-ray photoelectron spectroscopy (XPS) was employed to investigate the surface elemental composition and chemical valence states. During data collection, the pass energy was set to 20 eV, and the energy resolution was maintained at 0.05 eV. All binding energies were calibrated using the C 1s peak at 284.8 eV as the reference standard. The Shirley background was adopted for background subtraction. All XPS spectra were fitted and deconvoluted using standard Doniach-Sunjic functions to achieve quantitative analysis. The real and imaginary parts of dielectric loss and magnetic loss of composite materials were measured by using a Vector Network Analyzer (VNA, KeysightN5225B, USA).

RESULTS AND DISCUSSION

The flow chart for the synthesis of M-HHTP (M = Ni, Co) coordinated metal-organic framework materials by the solvothermal method in this study is shown in Figure 1A. In the solvothermal synthesis reaction, metal ions coordinate with the oxygen atoms on the HHTP ligand to form parallel structural units, and after crystal growth, the target M-HHTP cMOFs are formed[19,23,24]. From Figure 1B-G, it can be observed that there are rod-like structures and irregular crystals growing on the surface of these rod-like structures in the samples, and the rods and crystals in the images are clearly visible. Figure 1H-K and 1L-O show the energy dispersive X-ray spectroscopy (EDS) images of materials NCH1 and NCH3, and energy spectrum analysis of O, Co, and Ni elements was performed on samples NCH1 and NCH3, Confirming the existence of O, Co, and Ni elements in the materials. The distribution of the three elements can be observed in Figure 1K and O.

The crystallinity of cMOF can be further analysed by scanning M-HHTP using X-ray diffraction (PXRD). As can be seen in Figure 2A, the diffraction patterns at $2\theta = 9.22°$ and 13.94° correspond to the (200) and (210) crystal planes of Co-HHTP, confirming the successful synthesis of M-HHTP[25]. The XRD pattern of Ni-HHTP shows clear diffraction peaks at 9.22°, 13.94°, 16.1°, 21.3°, and 26.8°, which correspond to the (200), (210), (220), (221), and (004) crystal planes of Ni-HHTP[19,22]. It indicates that NCH1, NCH2 and NCH3 mainly maintain the crystal structure of Ni-HHTP. Only trace amounts of Co_3O_4 exist in the composite, which cannot be clearly observed in XRD patterns but leads to the obvious fluctuations of electromagnetic parameters of NCH2 as shown in Figure 2A. At the same time, characteristic peaks corresponding to metallic Ni, Co, or Ni-containing and Co-containing compounds were detected, indicating the samples have been synthesized successfully[26]. The elemental composition, chemical bonds, and chemical states of M-HHTP were examined by XPS. Figure 2B shows that the NCH1 sample exhibits peaks characteristic of C 1s, O 1s, Ni 2p and Co 2p, when taking NCH1 as an example. Figure 2C-F present the XPS spectra of sample NCH1, from which it can be seen that various diffraction peaks of C, O, Ni and Co exist in the bimetallic NCH1, confirming the presence of these elements. The C 1s XPS spectrum of sample NCH1 shows three peaks at 284.8, 286 and 288.5 eV, which correspond to C–C sp^3, C–O and O=C–O bonds, respectively[27]. The C–C/C=C sp^3 peaks are a result of the π-π conjugated benzene ring[28,29]. The O 1s XPS measurement displays two characteristic peaks, with the maximum peaks at 531.5 and 533.2 eV, respectively, correlating to the C–O and O=C–O groups[30,31]. Four characteristic peaks are observed in the Ni 2p XPS measurement spectrum. The absorption peaks observed at 853.7 and 873 eV are attributed to Ni $2p_{3/2}$ and Ni $2p_{1/2}$, indicating the presence of nickel in the compound. The peaks detected at 858 and 879 eV are consistent with the satellite peaks of Ni $2p_{3/2}$ and Ni $2p_{1/2}$, respectively[32,33]. The XPS spectroscopic analysis of Co 2p reveals the presence of five discernible peaks. The peaks at 778.2, 782 and 797.32 eV correspond to Co $2p_{3/2}$, Co-O and Co $2p_{1/2}$, respectively. The observed peaks at 785.7 and 803 eV correspond to the satellite peaks that have been previously identified.

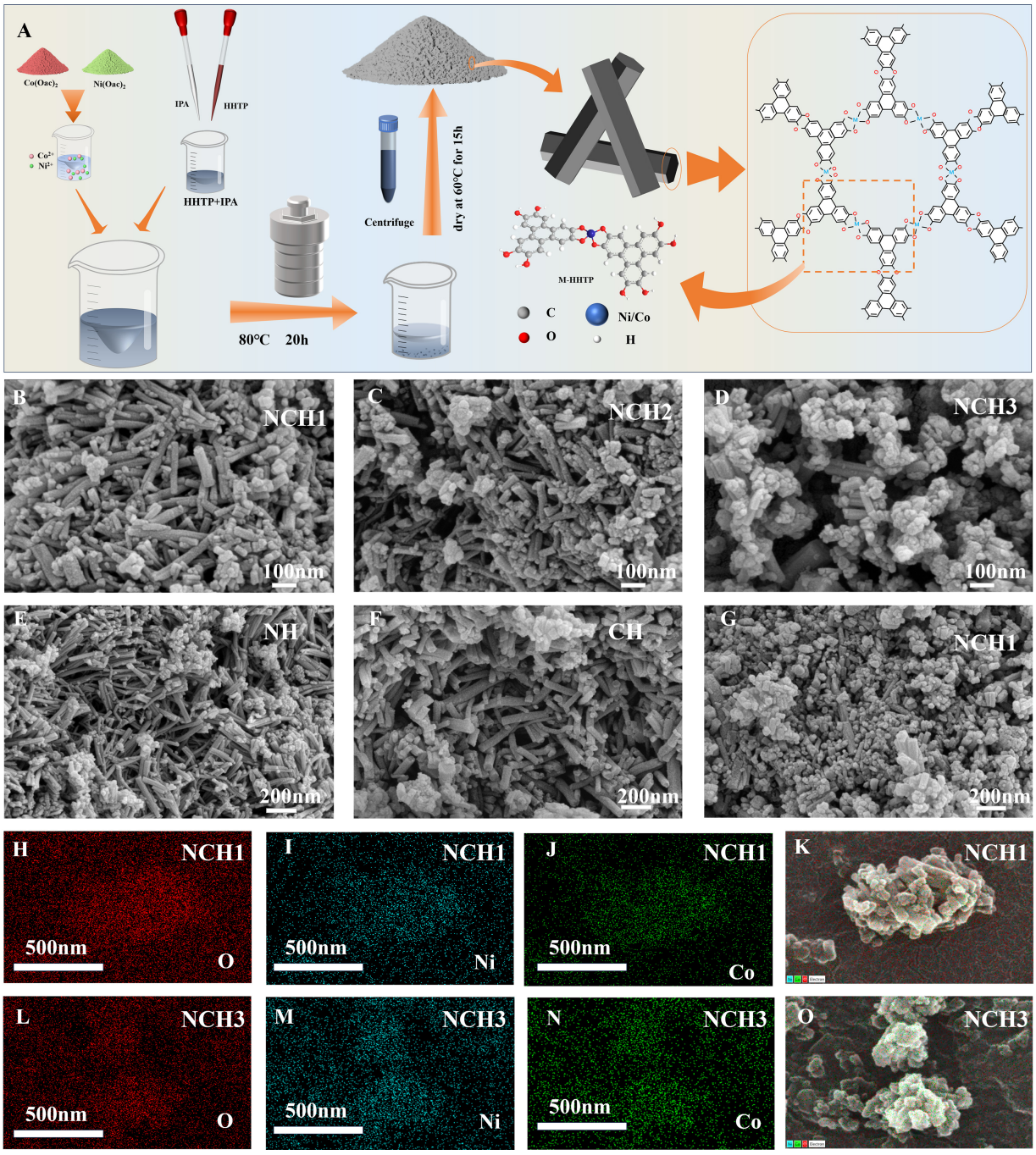

Figure 1. (A) shows a flow chart of how to prepare M-HHTP; (B-D) are the 100 nm SEM images of NCH1, NCH2 and NCH3, respectively; (E-G) are the 200 nm SEM images of NH, CH and NCH1, respectively; (H-K) are the EDS scans of O, Ni, Co and the three components in the material NCH1, respectively, and (L-O) are the EDS scans of O, Ni, Co and the three components in the material NCH3, respectively. HHTP: Hexahydroxytriphenylene; M-HHTP: metal-hexahydroxytriphenylene (M = Ni, Co); SEM: scanning electron microscopy; NCH1: nickel-cobalt hybrid material (Ni^{2+}:Co^{2+} = 1:3); NCH2: nickel-cobalt hybrid material (Ni^{2+}:Co^{2+} = 3:1); NCH3: nickel-cobalt hybrid material (Ni^{2+}:Co^{2+} = 1:1); EDS: energy dispersive X-ray spectroscopy; IPA: isopropanol; NH: nickel-only material; CH: cobalt-only material.

In accordance with the transmission line theory, the reflection loss (RL) parameters of the samples were calculated for the frequency band spanning 2 to 18 GHz, utilising the Equations (1) and (2)[34-36]. The outcomes of this calculation are presented in Figure 3. The microwave absorbing performance of the

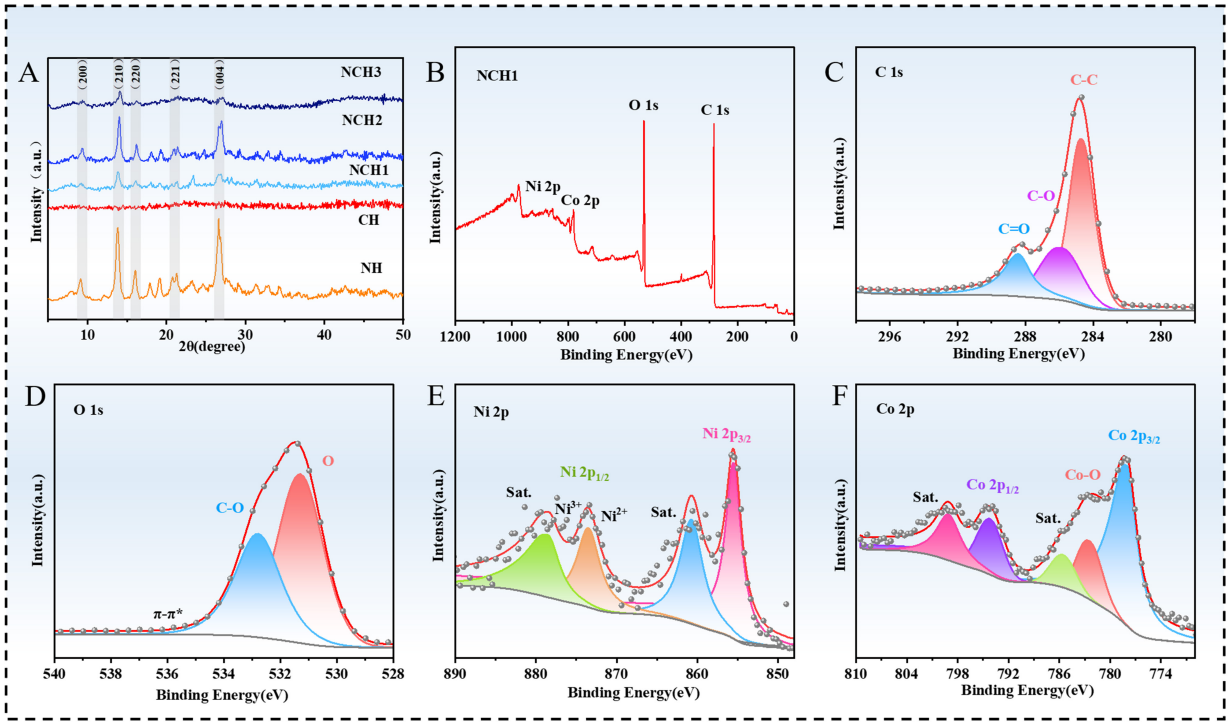

Figure 2. (A) shows the comparison of XRD patterns for NH, CH, NCH1, NCH2 and NCH3 samples; (B-F) show the XPS spectra measurements of C 1s, O 1s, Ni 2p and Co 2p for NCH1, respectively. XRD: X-ray diffraction; NH: nickel-only material; CH: cobalt-only material; NCH1: nickel-cobalt hybrid material (Ni^{2+}:Co^{2+} = 1:3); NCH2: nickel-cobalt hybrid material (Ni^{2+}:Co^{2+} = 3:1); NCH3: nickel-cobalt hybrid material (Ni^{2+}:Co^{2+} = 1:1); XPS: X-ray photoelectron spectroscopy.

prepared material samples was evaluated through RL and EAB (the frequencies covered when RL ≤ -10 dB)[37].

$$RL = 20\lg\left|\frac{Z_{in}-Z_0}{Z_{in}+Z_0}\right| \quad (1)$$

$$Z_{in} = Z_0\sqrt{\frac{\mu_r}{\varepsilon_r}}\tanh\left[j\left(\frac{2\pi fd}{c}\right)\sqrt{\mu_r\varepsilon_r}\right] \quad (2)$$

Here, Z_{in} is representative of the input impedance of the absorber, while Z_0 denotes the impedance in free space. The relative complex permittivity is denoted by ε_r, the relative complex permeability by μ_r, the variable f is the frequency of the incident EMW, d is the thickness, and c is the propagation speed of EMW in free space. Through the formula, we can understand the parameter relationships between Z_{in}, Z_0, ε_r, μ_r, f, d, and c. Figure 3A1, B1 and C1 illustrate the 3D RL variation curves of the respective samples. At the given matching thickness and frequency, the RL value of sample NCH3 is below the delineated contour line of -10 dB but always above -20 dB, indicating that the EWA of the bimetallic ions in material NCH3 under this ratio is insufficient. This makes the sample unable to effectively adjust the electromagnetic properties of the composite material, thereby leading to impedance mismatch. When incident electromagnetic waves occur, the presence of impedance mismatch leads to an increased number of reflections. This, in turn, reduces the energy absorbed inside the material, ultimately resulting in a more negative value of RL (i.e., stronger microwave absorption). As shown in Figure 3A1-A3 and B1-B3, when the thicknesses of samples NCH1 and NCH2 are 2.9 mm and 2.68 mm respectively, the RL_{min} values are -56.99 and -55.11 dB; when their thicknesses are 2.38 and 3.15 mm, the EAB reaches 6.51 and 6.16 GHz. This is due to the fact that, when the ratio of the bimetallic ions is Ni^{2+}:Co^{2+} = 1:3 and 3:1, composite material M-HHTP can effectively adjust the dielectric constant parameters and magnetic permeability parameters (ε_r and μ_r). This can

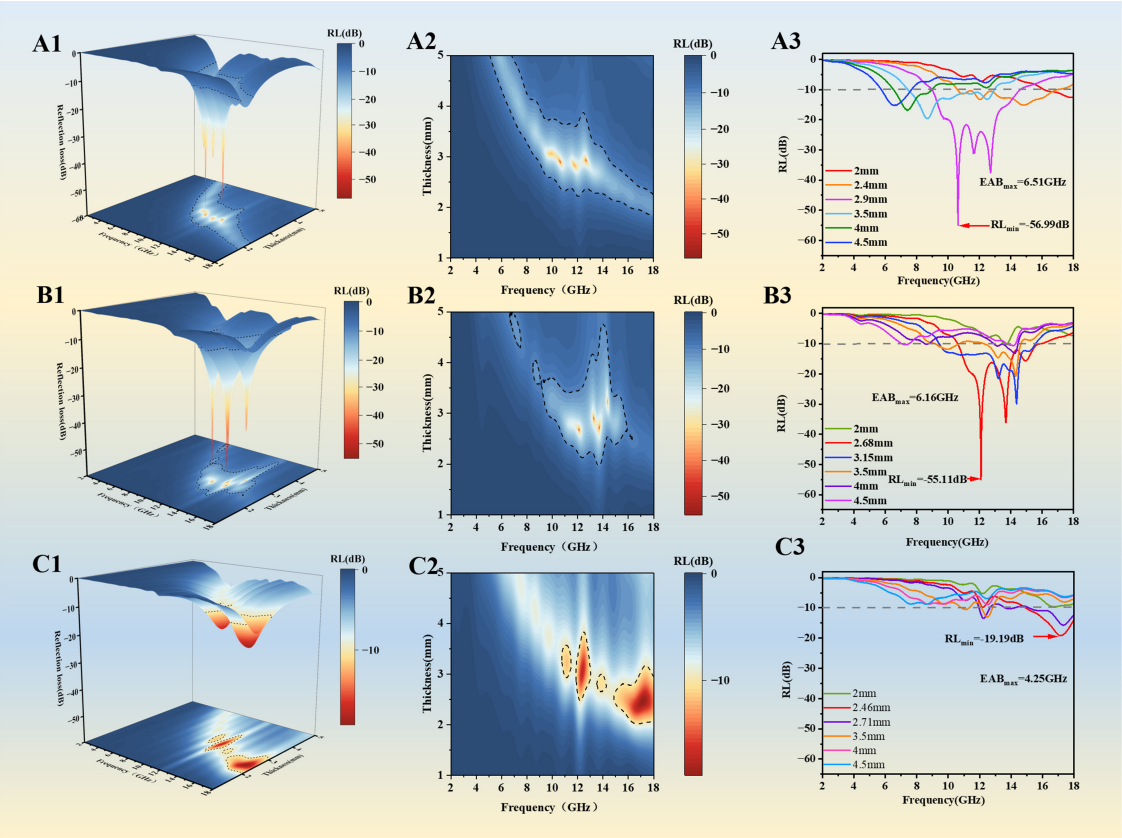

Figure 3. Analysis of the microwave absorption performance of M-HHTP; (A1-A3) are NCH1; (B1-B3) are NCH2; (C1-C3) are NCH3 3D and 2D RL value diagrams. M-HHTP: Metal-hexahydroxytriphenylene (M = Ni, Co); NCH1: nickel-cobalt hybrid material (Ni^{2+}:Co^{2+} = 1:3); NCH2: nickel-cobalt hybrid material (Ni^{2+}:Co^{2+} = 3:1); NCH3: nickel-cobalt hybrid material (Ni^{2+}:Co^{2+} = 1:1); 3D: three-dimensional; 2D: two-dimensional; RL: reflection loss; EAB_{max}: maximum effective absorption bandwidth; RL_{min}: minimum reflection loss.

therefore optimise impedance matching, reduce electromagnetic wave reflection, and improve energy absorption. Concurrently, the synergistic effect of both dipole polarization and interfacial polarization enhances energy conduction loss and facilitates optimised electron transport pathways, thereby achieving a lower RL value. M-HHTP, with the requisite thickness, can be utilised to optimise the electromagnetic characteristics of the constituent materials through the processes of polarization and dipole polarization, which are generated at the heterogeneous interface. This enhancement of impedance matching is achieved through a synergistic effect with mechanisms such as magnetic loss, thereby constructing a multiple loss system that encompasses "dielectric loss", "interface polarization", and "magnetic loss". This, in turn, results in a further reduction in the RL value.

Further studies were conducted on both the dielectric properties and magnetic permeability of sample M-HHTP, with EWA performance tests being carried out at elevated frequencies ranging from 2 to 18 GHz. Specifically, ε″ signifies the dissipative nature of the material under an applied electric field, whereas ε′ represents its inherent capacity for energy storage. The specific expressions of ε′ and ε″ are as follows[38,39]:

$$\varepsilon' = \varepsilon_\infty + \frac{\varepsilon_s - \varepsilon_\infty}{1+(2\pi f)^2\tau^2} \quad (3)$$

$$\varepsilon'' = \frac{2\pi f\tau(\varepsilon_s - \varepsilon_\infty)}{1+(2\pi f)^2\tau^2} \quad (4)$$

Here, ε_s represents the static dielectric constant, ε_∞ represents the relative dielectric constant, and τ represents the dielectric relaxation time. Dielectric loss is a form of manifestation of electromagnetic wave attenuation.

Conduction loss and dielectric polarization are the decisive factors of dielectric loss. In the electromagnetic wave frequency band, dielectric polarization includes interfacial polarization and dipole polarization. As illustrated in Figure 4A and B, the dielectric constant of NCH3 remains approximately constant at approximately 4 and 1.5 for the real and imaginary parts, respectively. In contrast, the real and imaginary parts of the dielectric constant of samples NCH1 and NCH2 exhibit a decrease with increasing frequency. The real part of the complex dielectric constant of NCH1 decreases from 8.5 to 5, and the imaginary part decreases from 2.5 to 1.5. However, the real part of the dielectric constant of NCH2 declines with rising frequency within the range of 2-14, and rises with increasing frequency within the range of 14-18. The imaginary component of the dielectric constant increases with rising frequency, within the 10-13 range, thereby signifying that polarization relaxation occurs within the samples at these specific frequencies. In addition, the ε′ and ε″ values of NCH1 are greater than those of NCH2 and NCH3, indicating that NCH1 has a higher ability to store and dissipate electric field energy than the other two bimetallic materials. In Figure 4C, it has been established that the dielectric loss tangent value of sample NCH1 is considerably higher than those of the two other samples, thus indicating that the dielectric loss of NCH1 is more significant in relation to that of the other samples. As shown in Figure 4D, NCH2 exhibits an obvious peak at approximately 10-14 GHz, with its μ′ rapidly rising to 1.45, indicating that the electromagnetic energy storage capacity of the material is significantly enhanced at this frequency. In contrast, the μ′ of NCH1 displays a gentle fluctuation within the range of 0.95-1.2 without the presence of discernible peaks, suggesting that its magnetic energy storage capacity remains relatively stable as the frequency increases, thus avoiding significant fluctuations. It is evident that the observed phenomenon is attributable to the natural resonance effect caused by Ni^{2+} and Co^{2+} within a distinct high-frequency range, specifically between 10 and 14 GHz[24]. The μ′ value of NCH2 shows obvious fluctuations at frequency 12, which is attributed to the coexistence of Co_3O_4 in the Co/C matrix. The different magnetic permeabilities and response frequencies of different magnetic phases cause specific phases to alternately dominate the magnetic response under different frequency bands, thereby inducing μ′ oscillations during the phase transition. It can be seen from Figure 4E that the μ″ values of NCH1 and NCH2 have large peaks at a frequency of 10-14 GHz, indicating that the samples have an enhanced magnetic loss effect in this frequency band[19,21]. However, at frequencies of 10-16, the μ″ values of NCH1 and NCH2 significantly increase from 0 to 0.3 and 0.5, indicating the appearance of obvious resonance peaks in these two frequency bands. The observation of this occurrence suggests that the magnetic dissipation is attributable to a combination of exchange and natural resonance. Figure 3F illustrates the magnetic loss ($\tan\delta_\mu = \mu'/\mu''$) value, which fluctuates between 0 and 0.4. It is evident that the $\tan\delta_\varepsilon$ value is considerably larger than the $\tan\delta_\mu$ value. This finding suggests that dielectric loss is a primary factor in the reduction of microwave energy[22,25,40]. Therefore, it can be concluded that the microwave energy attenuation of this sample is dominated by dielectric loss.

It is widely accepted that dielectric loss in microwave-absorbing materials (MAMs) can be categorised into two primary mechanisms: conductive and polarisation loss. The Debye theoretical model can further characterise the potential loss mechanisms in the sample[41,42]:

$$\left(\varepsilon' - \frac{\varepsilon_s - \varepsilon_\infty}{2}\right)^2 + (\varepsilon'')^2 = \left(\frac{\varepsilon_s - \varepsilon_\infty}{2}\right)^2 \quad (5)$$

In this equation, ε′ represents the real part of the dielectric constant, ε″ represents the imaginary part of the dielectric constant, ε_s stands for the static dielectric constant, and ε_∞ denotes the dielectric constant at the high-frequency limit. The Cole-Cole semicircle clearly characterises the polarisation relaxation process, with each distinct semicircle representing a separate polarisation relaxation mechanism, while the low-frequency linear tail region mainly arises from the contribution of conductive loss[43]. From the XRD pattern of sample A in Figure 2, it can be seen that, compared with other samples, NCH1 exhibits a higher degree of crystallinity, indicating the presence of more polarisation losses, including dipole polarisation of functional

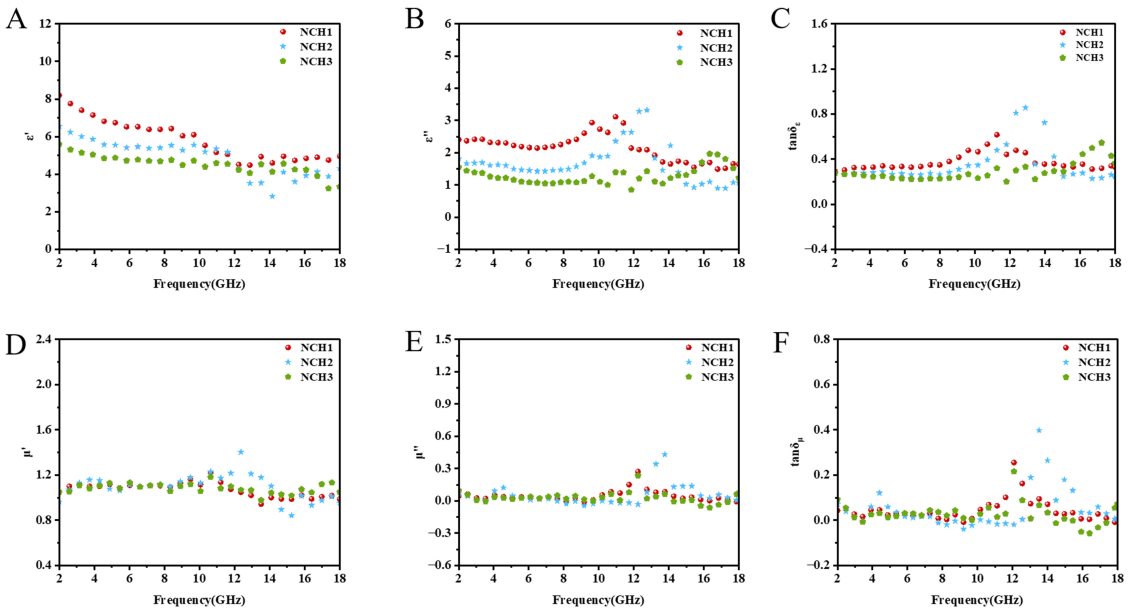

Figure 4. (A-F) are the analysis diagrams of the bimetallic electromagnetic loss mechanism of the samples; (A-C) are respectively the real part of the dielectric constant, the imaginary part of the dielectric constant, and the tangent of the dielectric loss angle corresponding to the frequency of the bimetal; (D-F) are the real part of permeability, the imaginary part of permeability, and the magnetic loss tangent corresponding to the frequency of the bimetal, respectively. NCH1: Nickel-cobalt hybrid material (Ni^{2+}:Co^{2+} = 1:3); NCH2: nickel-cobalt hybrid material (Ni^{2+}:Co^{2+} = 3:1); NCH3: nickel-cobalt hybrid material (Ni^{2+}:Co^{2+} = 1:1).

groups and unsaturated bonds, as well as bimetallic ions. The data in Figure 5A and B show that CH exhibits more Cole-Cole semicircles compared with NH. This research result confirms the following hypothesis: CH possesses stronger Debye dipole relaxation properties. Under the action of electromagnetic radiation, the polarization relaxation effect formed by electric dipoles composed of cobalt ions and oxygen atoms is stronger than that formed by electric dipoles composed of nickel ions and oxygen atoms. In addition, the data in Figure 5C-E indicates that NCH1 exhibits a greater number of Cole-Cole semicircles compared to NCH2 and NCH3. This finding points to the hypothesis that NCH1 displays stronger Debye dipole relaxation, attributable to the enhanced polarisation relaxation of the electric dipoles comprising nickel ions, cobalt ions, and oxygen atoms when exposed to electromagnetic wave radiation. To understand the relationship between NCH1 and thickness, RL, and frequency, we applied the quarter-wavelength theory, with the formula as follows:

$$t_m = \frac{nc}{4f_m \,\mathrm{Re}(\sqrt{\mu_r \varepsilon_r})} (n = 1, 3, 5, 7 \cdots) \quad (6)$$

The thickness is represented by t_m and the frequency by f_m. If the values of t_m and f_m satisfy Equation (6), then the interference of the incident and reflected waves cancels them out. At this point, the microwaves are absorbed by the material significantly more efficiently. Figure 5F shows the quarter-wavelength matching curve of NCH1. As can be seen, the peak of RL_{min} shifts towards the lower frequency range. This shift, caused by an increase in thickness, indicates that EMW at different frequency bands can be achieved by adjusting the material thickness. The red curve in the figure shows the t_m values that were calculated using the t theoretical model of a quarter wavelength. The intersection of the extended line of the RL_{min} peak with the extended line of the t_m value aligns well with the 1/4 λ curve, indicating that the interference effect also contributes to the absorption performance of NCH1. Furthermore, filler loading and sample thickness jointly determine the final microwave absorption performance. In this work, under a fixed filler loading of 50 wt%, the composite possesses suitable conductivity and moderate dielectric loss, avoiding impedance mismatch caused by excessively high or low filling content. When the matching thickness reaches 2.9 mm, it satisfies

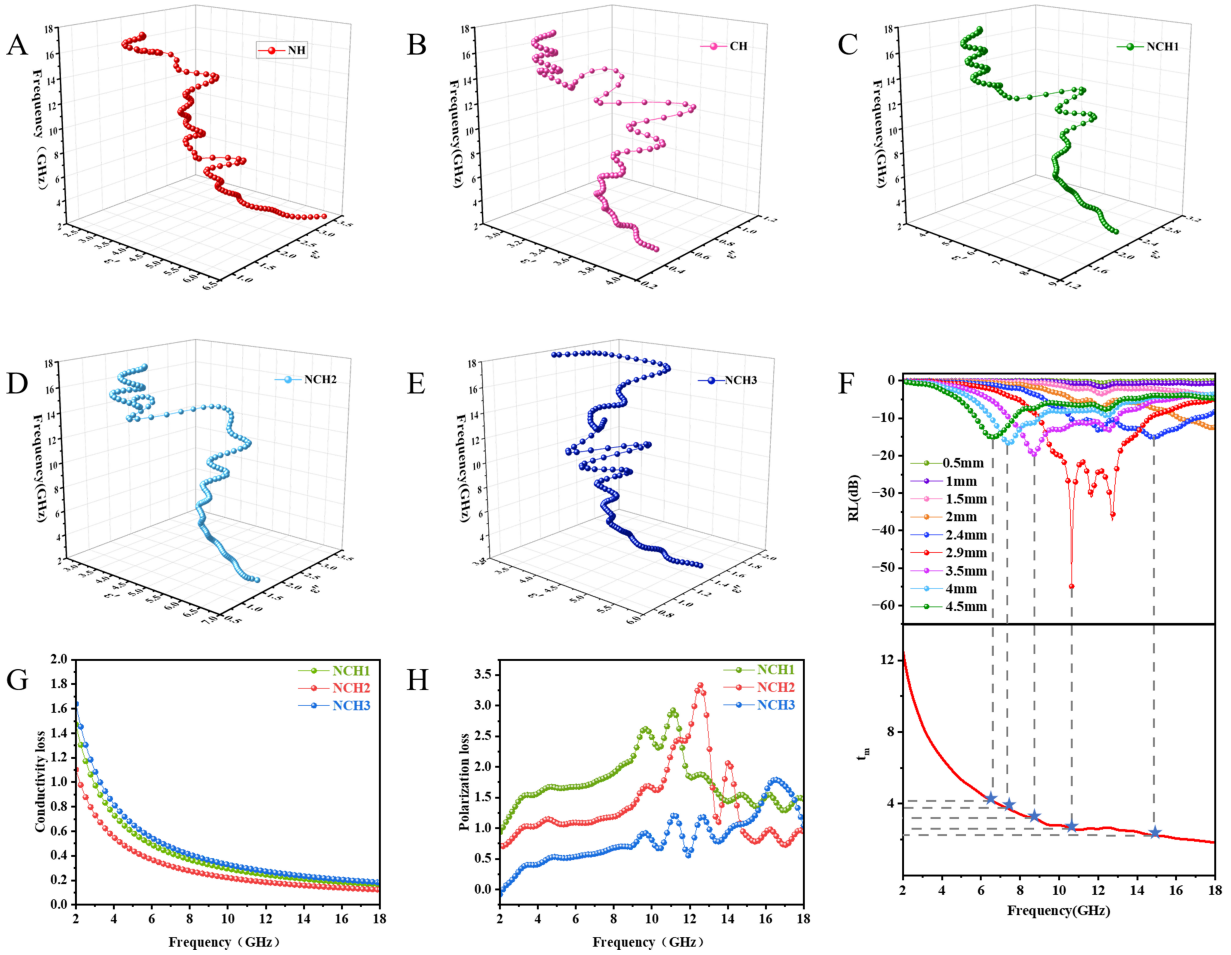

Figure 5. (A-E) shows the Cole-Cole curves of NH, CH, NCH1, NCH2 and NCH3; (F) shows the RL values of NCH1 related to frequency and thickness, the pentagrams indicate that the frequencies corresponding to the RL values of different thicknesses exactly fall on the λ/4 frequency curve; (G) represents conductive loss (ε_c''); (H) represents polarisation loss (ε_p''). NH: Nickel-only material; CH: cobalt-only material; NCH1: nickel-cobalt hybrid material (Ni^{2+}:Co^{2+} = 1:3); NCH2: nickel-cobalt hybrid material (Ni^{2+}:Co^{2+} = 3:1); NCH3: nickel-cobalt hybrid material (Ni^{2+}:Co^{2+} = 1:1); RL: reflection loss.

the quarter-wavelength attenuation principle and realizes optimal impedance matching with free space. Consequently, the NiCo-HHTP composite delivers an excellent reflection loss value of -56.99 dB at this condition.

Using the Debye relaxation formula in conjunction with nonlinear fitting via the least squares method, Equations (7) and (8) can be used to calculate ε_p'' and ε_c''[43]:

$$\varepsilon_c'' = \frac{\sigma}{2\pi f \varepsilon_0} \tag{7}$$

$$\varepsilon_p'' = (\varepsilon_s - \varepsilon_\infty) \frac{2\pi f \tau}{1+(2\pi f)^2 \tau^2} \tag{8}$$

As shown in Figure 5G and H, the two types of losses exhibit opposite trends with frequency: ε_c gradually decreases, while ε_p increases with increasing frequency. This indicates that the concentration of ε_c is primarily observed within the low-frequency range, while the predominance of ε_p is seen in the high-frequency range. Furthermore, as the amount of Co^{2+} decreases and Ni^{2+} increases, both ε_p and ε_c decrease. In NCHX composites, the conductivity effect of Co–C bonds formed by Co^{2+} with semiconductor characteristics

combining with C atoms is inferior to that of Ni-C bonds formed by Ni^{2+} combining with C atoms, which hinders the effective transmission of active electrons, resulting in low conductivity. However, this does not affect the EMW absorption of composites with other proportions (such as NCH2). NCH2 forms numerous heterojunction surfaces where heterocharges accumulate to create dipole polarisation, which, through interaction with interfacial polarisation, weakens EMW[44].

The parameters of impedance matching |Z| and attenuation constant α are fundamental to the classification of effective wave-absorbing materials, as evidenced by the following formulae[19]:

$$|Z| = (\mu_r/\varepsilon_r)^{1/2} \tag{9}$$

$$\alpha = \frac{\sqrt{2}\pi f}{c}\sqrt{(\mu''\varepsilon'' - \mu'\varepsilon')^2 + \sqrt{(\mu''\varepsilon'' - \mu'\varepsilon')^2 + (\mu'\varepsilon'' + \mu''\varepsilon')^2}} \tag{10}$$

Here, c is the speed of light in a vacuum. The absorbing material's attenuation capability is directly proportional to the size of the attenuation constant. Impedance matching value of 1 means more electromagnetic waves are absorbed, leading to larger α values and stronger dissipation. As illustrated in Figure 6A and B, within the 2-8 frequency range, the highest impedance matching is evident in NCH1, indicating its capacity to absorb a significant volume of low-frequency electromagnetic energy. Its attenuation capability for low-frequency electromagnetic waves is notably efficacious. However, the NCH1 sample exhibits the poorest impedance matching for electromagnetic waves within the 10-18 GHz frequency range. The NCH1 sample absorbs more mid-frequency electromagnetic waves (8-13) and exhibits higher attenuation capability than the NCH2 and NCH3 samples, converting them into other forms of energy. In the frequency region spanning from 8 to 12, the highest observed impedance matching is exhibited by NCH2, suggesting its capacity to absorb and convert a substantial proportion of mid-frequency electromagnetic waves. Furthermore, its attenuation capability for electromagnetic waves within the 12-14 mid-frequency range is particularly pronounced, indicating its optimal performance in this spectral domain. In summary, achieving high electromagnetic wave absorption performance requires a good balance between the material's impedance matching |Z| and the attenuation constant α. To further highlight the advantages of NiCo-HHTP, its absorption mechanisms are systematically compared with classic representative 2D materials such as graphene, MXenes, and other 2D conductive MOFs. Compared with graphene and MXene, which usually exhibit excessively high conductivity and poor impedance matching[45,46], the 2D NiCo-HHTP framework optimally balances dielectric loss and magnetic loss through bimetallic modulation[22,47]. Different from single-component 2D MOF materials with limited loss sources, the prepared NiCo-HHTP simultaneously integrates interfacial polarization relaxation, magnetic resonance loss, and thermal conversion effects. Such a multi-mechanism collaborative system endows NiCo-HHTP with more superior impedance matching characteristics and stronger electromagnetic attenuation capability, thereby demonstrating obvious competitive advantages over conventional 2D wave-absorbing materials.

To further investigate the mechanism of magnetic loss, we introduce the eddy current loss C_0 for analysis, which is expressed as follows[48]:

$$C_0 = \mu''(\mu')^2 f^{-1} \tag{11}$$

When identified as the primary cause of magnetic loss, eddy current loss is expected to exhibit relatively stable C_0 values across different frequencies. Conversely, deviations in C_0 can be ascribed to natural resonance or exchange resonance phenomenon. For samples NCH1 and NCH2 in the 5-12 GHz frequency range, the curves show minimal oscillation, indicating that magnetic loss is primarily governed by eddy current effects in this region [Figure 6C]. In accordance with Aharoni's theory, it is acknowledged that

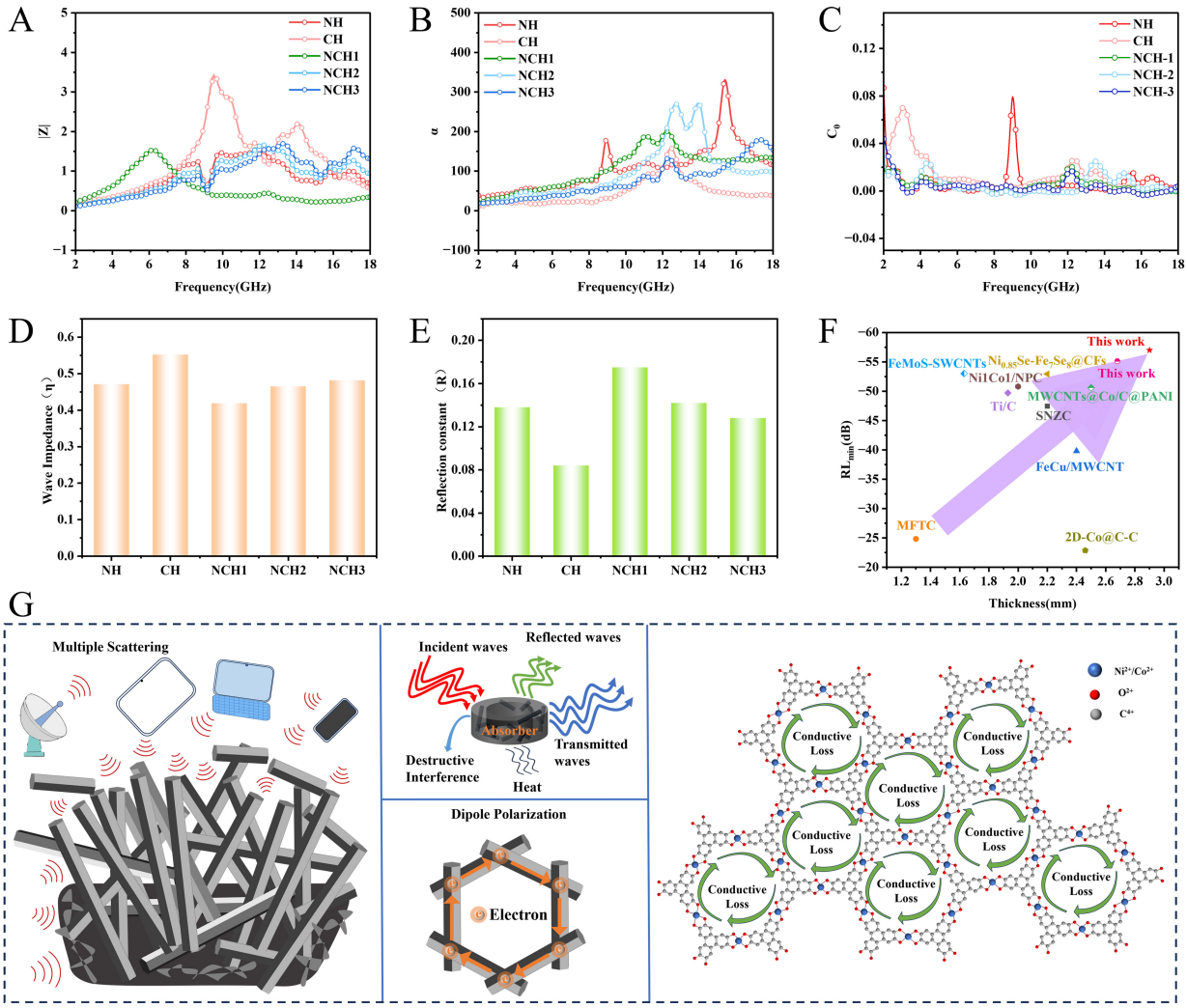

Figure 6. (A) shows the impedance matching |Z| value and (B) shows the attenuation constant α value; (C) Eddy current loss; (D) Wave impedance (η); (E) Reflection coefficient (R); (F) Comparison with other similar absorbing materials (data source Table 1); (G) The electromagnetic wave absorption mechanism of M-HHTP is explained here. NH: Nickel-only material; CH: cobalt-only material; NCH1: nickel-cobalt hybrid material (Ni^{2+}:Co^{2+} = 1:3); NCH2: nickel-cobalt hybrid material (Ni^{2+}:Co^{2+} = 3:1); NCH3: nickel-cobalt hybrid material (Ni^{2+}:Co^{2+} = 1:1).

exchange resonance manifests at frequencies that surpass those of natural resonance[49]. It is evident that natural resonance is predominantly exhibited within the lower frequency range of 2-5 GHz, while exchange resonance assumes a principal role within the higher frequency range of 12-18 GHz.

Under normal circumstances, impedance is determined by frequency, wavelength and thickness. The fixed impedance matching characteristics of the material can be represented by the wave impedance (η). As shown in Figure 6D, η varies with the ratio of Ni^{2+} and Co^{2+}, increasing from 0.42 for NCH1 (Ni^{2+}:Co^{2+} = 1:3) to 0.47 for NCH2 (Ni^{2+}:Co^{2+} = 3:1) and 0.48 for NCH3 (Ni^{2+}:Co^{2+} = 1:1). This indicates that composites modified with different ratios can enhance η. The reflection coefficient (R) of the material is shown in Figure 6E. The reflection coefficient R shows an opposite trend to the impedance matching coefficient η. Although NCH1 exhibits the largest real part of R, the magnitude of its reflection coefficient |R| is only 0.18. The |R| values of all composites are less than 0.2, indicating that the reflection of EMW by the composites is weak and well within an acceptable range. It has been clarified that NCH1 exhibits the magnitude of the reflection coefficient |R| only 0.18, which is fully consistent with its optimum RL_{min} =-56.99 dB and superior microwave

Table 1. Comparison of EMW absorption properties

Sample	RL_{min} (dB)	t_m (mm)	EAB (GHz)	t_m (mm)	References
Ti/C	-49.7	1.93	4.16	2.2	[50]
MWCNTs@Co/C@PANI	-50.6	2.5	7.09	/	[40]
MFTC	-24.83	1.3	4.72	1.5	[51]
FeCu/MWCNT	-39.82	2.4	9.63	1.8	[52]
SNZC	-47.43	2.20	14.8	/	[53]
$Ni_{0.85}Se$-Fe_7Se_8@CFs	-52.93	2.2	7.12	2.0	[54]
FeMoS-SWCNTs	-53.01	1.63	5.20	1.72	[55]
Ni_iCo_i/NPC	-50.8	2	4.56	/	[56]
2D-Co@C-C	-22.87	2.46	6.41	1.82	[57]
NCH1	-56.99	2.9	6.51	2.38	This work
NCH2	-55.11	2.68	6.16	3.15	This work

EMW: Electromagnetic waves; RL_{min}: minimum reflection loss; EAB: effective absorption bandwidth; MWCNTs: multi-walled carbon nanotubes; PANI: polyaniline; MFTC: multiple interfacial magnetic carbon foams; MWCNT: multi-walled carbon nanotube; SNZC: SiO_2@C@void@$Ni_3ZnC_{0.7}$/C; CFs: carbon fibers; FeMoS-SWCNTs: FeS/MoS_2@N-doped carbon sandwich-walled nanotubes; NPC: porous carbon/magnetic metal particle composites; 2D: two-dimensional; NCH1: nickel-cobalt hybrid material (Ni^{2+}:Co^{2+} = 1:3); NCH2: nickel-cobalt hybrid material (Ni^{2+}:Co^{2+} = 3:1).

absorption performance. Surprisingly, although NCH3 has the lowest reflection coefficient, its minimal reflection loss is less than the minimal reflection losses of NCH1 and NCH2. This is because excellent wave-absorbing materials are determined by the interaction of impedance matching and attenuation intensity. To highlight the superiority of NCH1 and NCH2 in wave absorption and energy absorption, NCH1 and NCH2 were compared with previously reported similar wave-absorbing materials, as shown in Figure 6F. The prepared NCH1 and NCH2 materials exhibit a strong reflection absorption effect, and their performance is significantly superior to other similar wave-absorbing materials.

Figure 6F compares the cMOF of this study with other previously reported wave-absorbing materials of the same type (the data are shown in Table 1), thereby highlighting the superiority of the MOF prepared in this research. In Table 1, the left t_m corresponds to the thickness at RL_{min} (dB), and the right t_m corresponds to the matching thickness at EAB (GHz). Both the RL value and EAB are comparable to those of MOF derivatives and typical dielectric materials. This excellent performance is contributed by the conjugation effect, abundant end groups and shape anisotropy, which can enhance conductive loss and promote polarization loss. Figure 6G illustrates in detail the electromagnetic wave absorption mechanism of NCHx. The optimal ratio between Ni^{2+} and Co^{2+} can adjust the electromagnetic parameters, thereby achieving excellent impedance matching performance. This allows electromagnetic waves to effectively penetrate the absorber. The rod-like morphology and surface-grown unit cells promote multiple scattering and reflection of electromagnetic waves within the absorber, increasing their attenuation path. Although Co^{2+} and Ni^{2+} with semiconductor characteristics can hinder the transport of active electrons in the sample, NH and CH with high dielectric performance, after co-doping with Co^{2+} and Ni^{2+}, can provide better dielectric loss. In an alternating electric field environment, the abundant heterojunction surfaces and numerous defect dipoles present in the bimetallic rod-like NCH1 and NCH2 play a positive role in enhancing ε_p''. Finally, magnetic loss is generated on electromagnetic waves through natural resonance, exchange resonance, and eddy current loss. Under the combined effect of these abundant electromagnetic wave absorption mechanisms, NCH1 exhibits the most outstanding wave absorption performance.

Based on the excellent wave-absorbing performance obtained from electromagnetic parameter tests, the radar cross section (RCS) of metal substrates coated with NH, CH and NCH1, NCH2, NCH3 absorbing materials, as well as that of an ideal square conductor, was simulated using computer simulation technology

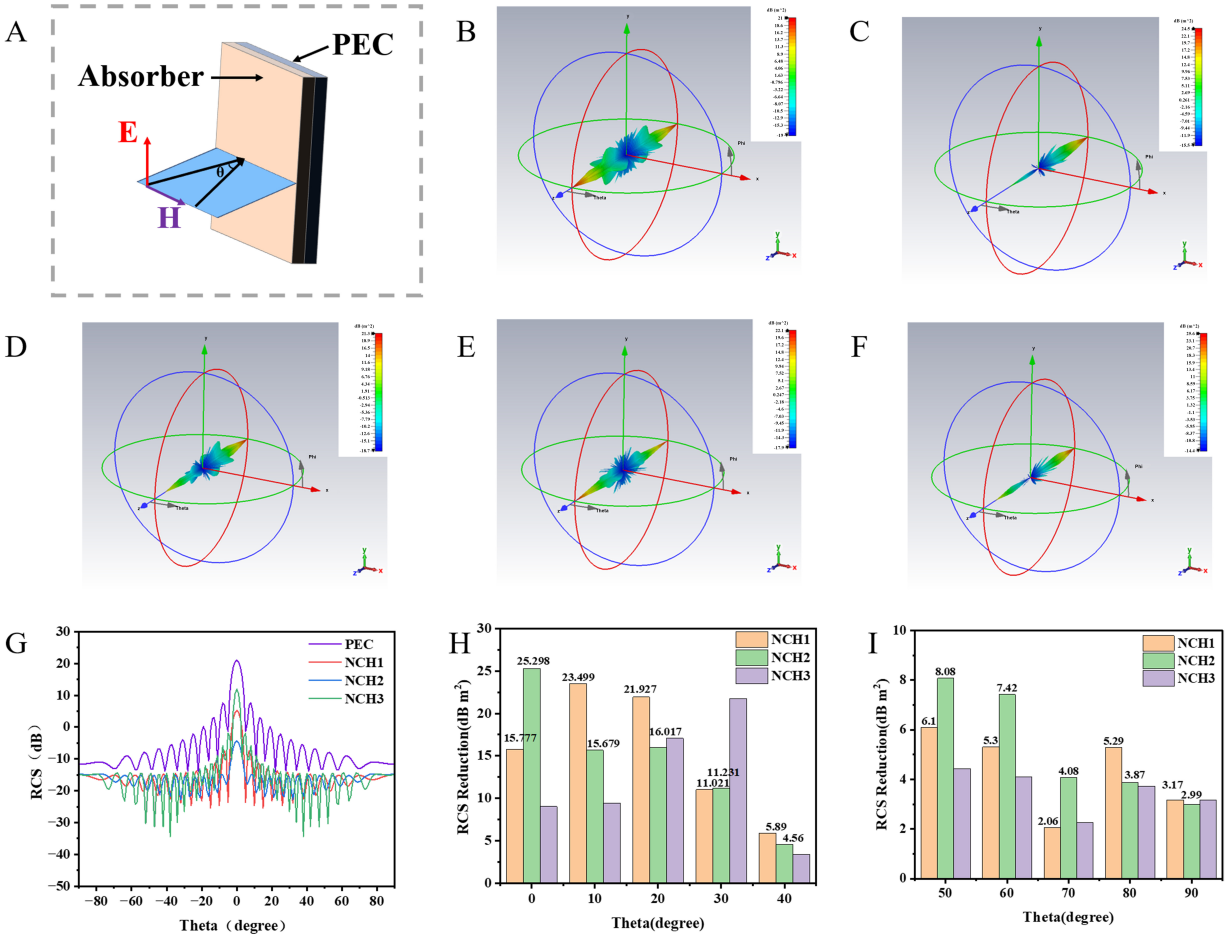

Figure 7. (A) CST simulation model; (B-F) RCS simulation results of PEC, NH, CH, NCH1, NCH2, and NCH3 at different scanning angles; (G) RCS simulation curves; (H and I) Comparative analysis of the RCS recovery values of each sample. CST: Computer simulation technology; RCS: radar cross section; PEC: perfect electric conductor; NH: nickel-only material; CH: cobalt-only material; NCH1: nickel-cobalt hybrid material (Ni^{2+}:Co^{2+} = 1:3); NCH2: nickel-cobalt hybrid material (Ni^{2+}:Co^{2+} = 3:1); NCH3: nickel-cobalt hybrid material (Ni^{2+}:Co^{2+} = 1:1).

(CST) Studio Suite 2024 [Figure 7A]. This simulation verified the actual stealth performance of the absorbing materials[43,58]. Figure 7B-F show the simulation results used to visualise the sample's attenuation capability. The perfect electric conductor (PEC) plate coated with NCH1 exhibits an extremely weak RCS signal, confirming its excellent absorption performance. Figure 7G shows that this PEC plate has the strongest signal scattering characteristics. Compared with PEC plates coated with NCH1, NCH2, and NCH3 absorptive materials, its RCS values are reduced to varying degrees. This indicates that the absorptive coatings have good EMW attenuation capabilities, with the PEC plate coated with NCH2 having the lowest RCS value, corresponding to its optimal reflection loss. Furthermore, the signal attenuation of each absorptive material relative to the PEC plate was calculated. As shown in Figure 7H and I, when EMW is incident vertically, the attenuation value of NCH2 reaches 25.298 dB·m², indicating that this material has a significant attenuation effect on electromagnetic waves at this angle of incidence.

CONCLUSION

This research system explores the effects of the ratio of different magnetic central metals in Metal-organic Frameworks on the morphology, structure and electromagnetic parameters of materials, and further investigates the mechanism of electromagnetic synergism on wave absorption performance. The study finds that reasonable regulation of asymmetric central metals in the bimetallic structure can induce intrinsic

electromagnetic synergistic effects of the materials. That is, a synergistic interaction occurs between dielectric loss and magnetic loss to enhance energy dissipation, thereby achieving lower reflection loss values. This research provides a novel approach for the design of high-efficiency electromagnetic wave absorbing materials. Follow-up research will focus on microstructure regulation and composite system expansion to promote the research and development progress of bimetallic organic framework-based wave absorbing materials.

DECLARATIONS

Authors' contributions

Writing - original draft preparation: Luo, K.
Writing - review and editing: Luo, K.; Hu, Y.
Texting: Lu, M.; Lei, Z.
Supervision: Zhou, T.; Zhang, D.; Liu, X.; Gong, W.

Availability of data and materials

The data supporting the findings of this study are available from the corresponding author upon reasonable request.

AI and AI-assisted tools statement

Not applicable.

Financial support and sponsorship

This study was financially supported by the National Natural Science Foundation of China Project (52163001), Guizhou Provincial Science and Technology Plan Project (Qiankehe Platform Talent-GCC[2022]010-2, Qiankehe Zhongyindi [2024]042, Qiankehe Jichu-ZK[2024]YB488, Qiankehe Zhongyindi [2025]013, Qiankehe Results [2025]109,Qiankehe Talent XKBF[2025]005), Guizhou Provincial Scientist Workstation (Qiankehe Platform KXJZ[2024]022),Guiyang Baiyun District Science and Technology Plan Project (Grant No. baikehetong[2025]4) Guizhou Provincial Department of Education Hundred Universities, Thousand Enterprises Science and Technology Challenge Project(Qian Jiao Ji [2025] No. 007), Doctor Startup Fund of Guizhou Minzu University (Grant No. GZMUZK[2024]QD77), Guiyang Baiyun District Science and Technology Plan Project (Grant No. baikehetong[2025]3).

Conflicts of interest

All authors declared that there are no conflicts of interest.

Ethical approval and consent to participate

Not applicable.

Consent for publication

Not applicable.

REFERENCES

1. Cheng, J.; Zhang, H.; Ning, M.; et al. Emerging materials and designs for low- and multi-band electromagnetic wave absorbers: the search for dielectric and magnetic synergy? *Adv. Funct. Mater.* **2022**, *32*, 2200123. DOI
2. Iqbal, A.; Sambyal, P.; Koo, C. M. 2D MXenes for electromagnetic shielding: a review. *Adv. Funct. Mater.* **2020**, *30*, 2000883. DOI
3. Wang, Z.; Li, W.; Feng, L.; et al. Machine learning driven window blinds inspired porous carbon-based flake for ultra-broadband electromagnetic wave absorption. *Adv. Sci.* **2026**, *13*, e21130. DOI PubMed PMC
4. Wang, B.; Huang, J.; Liu, G.; et al. Design and optimization oriented composition and morphology engineering for MOF derived microwave absorbents. *Nano. Mater. Sci.* **2025**, S2589965124001594. DOI

5. Zhang, K.; Liu, Y.; Liu, Y.; et al. Tracking regulatory mechanism of trace fe on graphene electromagnetic wave absorption. *Nano-Micro. Lett.* **2024**, *16*, 66. DOI PubMed PMC
6. Tao, J.; Sugumaran, P. J.; Zhao, Y.; et al. Cascaded built-in electric fields engineering for electromagnetic wave absorption. *Adv. Mater.* **2026**, *38*, e23404. DOI PubMed
7. Liu, J.; Zhang, L.; Wu, H. Anion-doping-induced vacancy engineering of cobalt sulfoselenide for boosting electromagnetic wave absorption. *Adv. Funct. Mater.* **2022**, *32*, 2200544. DOI
8. Yi, C.; Hu, J.; Wang, J.; et al. Dual magnetic resonances from site-selective doping of hexaferrite yielding ultrabroadband microwave absorption. *Adv. Mater.* **2025**, *38*, e16331. DOI PubMed
9. Kang, G.; Kwon, G.; Jeon, J.; et al. Electromagnetic interference shielding using metal and MXene thin films. *Nature* **2025**, *647*, 356-63. DOI PubMed
10. Lv, H.; Yao, Y.; Li, S.; et al. Staggered circular nanoporous graphene converts electromagnetic waves into electricity. *Nat. Commun.* **2023**, *14*, 1982. DOI PubMed PMC
11. Miao, P.; Zhou, R.; Chen, K.; Liang, J.; Ban, Q.; Kong, J. Tunable electromagnetic wave absorption of supramolecular isomer-derived nanocomposites with different morphology. *Adv. Mater. Interfaces.* **2020**, *7*, 1901820. DOI
12. Yang, Q.; Chen, P.; Li, X.; Zhu, Y. Rational design of SiBCN ceramics with excellent attenuation to strong electromagnetic-wave-absorbing properties at low frequency. *Compos. Part. B. Eng.* **2024**, *280*, 111486. DOI
13. Wu, Z.; Cheng, H. W.; Jin, C.; et al. Dimensional design and core-shell engineering of nanomaterials for electromagnetic wave absorption. *Adv. Mater.* **2022**, *34*, 2107538. DOI PubMed
14. Geng, T. B.; Yu, G. Y.; Shao, G. F.; Huang, X. G. Enhanced electromagnetic wave absorption properties of ZIF-67 modified polymer-derived SiCN ceramics by *in situ* construction of multiple heterointerfaces. *Rare. Met.* **2023**, *42*, 1635-44. DOI
15. Xu, C.; Ding, J.; Luo, K.; et al. Dielectric-magnetic synergized pores modulation engineering in polymer aerogels for integrated electromagnetic wave absorption and infrared stealth. *Compos. Sci. Technol.* **2026**, *277*, 111552. DOI
16. Ma, X.; Tan, L.; Xu, J.; Hao, J. Co-Ni/C composite derived from N, S-codoped graphene decorate metal-organic framework toward microwave attenuation. *Langmuir* **2025**, *41*, 3684-94. DOI PubMed
17. Zhang, G.; Jin, L.; Zhang, R.; Bai, Y.; Zhu, R.; Pang, H. Recent advances in the development of electronically and ionically conductive metal-organic frameworks. *Coord. Chem. Rev.* **2021**, *439*, 213915. DOI
18. Wu, C.; Geng, P.; Zhang, G.; Li, X.; Pang, H. Synthesis of conductive MOFs and their electrochemical application. *Small* **2023**, *20*, 2308264. DOI PubMed
19. Shan, Z.; Cheng, S.; Wu, F.; et al. Electrically conductive two-dimensional metal-organic frameworks for superior electromagnetic wave absorption. *Chem. Eng. J.* **2022**, *446*, 137409. DOI
20. Zhang, X.; Tian, X. L.; Qin, Y.; et al. Conductive metal-organic frameworks with tunable dielectric properties for boosting electromagnetic wave absorption. *ACS. Nano.* **2023**, *17*, 12510-8. DOI PubMed
21. Chen, C.; Shan, Z.; Tao, S.; et al. Atomic tuning in electrically conducting bimetallic organic frameworks for controllable electromagnetic wave absorption. *Adv. Funct. Mater.* **2023**, *33*, 2305082. DOI
22. Zhang, X.; Qiao, J.; Wu, N.; et al. Conductive bimetal-organic frameworks with volcano-type fine-tuned dielectric properties for electromagnetic wave absorption. *ACS. Nano.* **2025**, *19*, 26761-9. DOI PubMed
23. Yang, X.; Yi, J.; Wang, T.; et al. Wet-adhesive on-skin sensors based on metal-organic frameworks for wireless monitoring of metabolites in sweat. *Adv. Mater.* **2022**, *34*, 2201768. DOI PubMed
24. Lu, G.; Zong, B.; Tao, T.; Yang, Y.; Li, Q.; Mao, S. High-performance $Ni_3(HHTP)_2$ film-based flexible field-effect transistor gas sensors. *ACS. Sens.* **2024**, *9*, 1916-26. DOI PubMed
25. Hoyos-sinchi, V.; Souza, P. H.; Orellana, W. Computational insights into two-dimensional $M_3(HHTP)_2$ metal-organic frameworks as ORR/OER electrocatalysts. *J. Phys. Chem. C.* **2025**, *129*, 14002-10. DOI
26. Li, J.; Huang, Y.; Zhou, Y.; et al. Controllable construction of two-dimensional conductive $M_3(HHTP)_2$ nanorods for electrochemical sensing of malachite green in fish. *ACS. Appl. Nano. Mater.* **2023**, *6*, 22916-26. DOI
27. Mishakov, I. V.; Bauman, Y. I.; Brzhezinskaya, M.; et al. Water purification from chlorobenzenes using heteroatom-functionalized carbon nanofibers produced on self-organizing Ni-Pd catalyst. *J. Environ. Chem. Eng.* **2022**, *10*, 107873. DOI
28. Nazir, A.; Le, H. T.; Nguyen, A.; Kim, J.; Park, C. Conductive metal organic framework mediated Sb nanoparticles as high-capacity anodes for rechargeable potassium-ion batteries. *Chem. Eng. J.* **2022**, *450*, 138408. DOI
29. Deshmukh, S.; Jakobczyk, P.; Pyrchla, K.; et al. Laser-induced heterostructuring of graphene passivated nanoscale black phosphorus frameworks for lithium-ion battery anodes. *Small* **2025**, *21*, e04480. DOI PubMed PMC
30. Wang, Y.; Zhao, J.; Wu, F.; et al. An ordered conductive Ni-CAT nanorods array as all-round polysulfide regulator for lithium-sulfur batteries. *Electrochim. Acta.* **2023**, *441*, 141788. DOI

31. Khodadadiyazdi, M.; Ficek, M.; Brzhezinskaya, M.; et al. Robust laser-induced graphene-boron-doped diamond nanowall hybrid nanostructures with enhanced field electron emission performance for microplasma illumination devices. *Small. Sci.* **2025**, *5*, 2400430. DOI PubMed PMC
32. Wu, T.; Ren, F.; Guo, Z.; et al. Hierarchical assembly of ternary MOF-derived sandwich composites for high-efficiency tunable electromagnetic wave absorption. *Small* **2024**, *20*, 2407599. DOI PubMed
33. Liu, M.; Wei, J.; Lin, S.; Cai, Z. Triggering anodic luminol electrochemiluminescence through electrostatic interactions: an innovative approach utilizing conductive metal-organic framework Co-HHTP. *ACS. Appl. Electron. Mater.* **2024**, *6*, 2375-82. DOI
34. Han, Y.; He, M.; Hu, J.; et al. Hierarchical design of FeCo-based microchains for enhanced microwave absorption in C band. *Nano. Res.* **2022**, *16*, 1773-8. DOI
35. Sun, L.; Zhu, Q.; Jia, Z.; Guo, Z.; Zhao, W.; Wu, G. CrN attached multi-component carbon nanotube composites with superior electromagnetic wave absorption performance. *Carbon* **2023**, *208*, 1-9. DOI
36. Wang, C.; Liu, Y.; Jia, Z.; Zhao, W.; Wu, G. Multicomponent nanoparticles synergistic one-dimensional nanofibers as heterostructure absorbers for tunable and efficient microwave absorption. *Nano-Micro. Lett.* **2022**, *15*, 13. DOI PubMed PMC
37. Zhao, J.; Wei, Y.; Zhang, Y.; Zhang, Q. 3D flower-like hollow CuS@PANI microspheres with superb X-band electromagnetic wave absorption. *J. Mater. Sci. Technol.* **2022**, *126*, 141-51. DOI
38. Liang, Q.; Wang, L.; Qi, X.; et al. Hierarchical engineering of CoNi@Air@C/SiO_2@Polypyrrole multicomponent nanocubes to improve the dielectric loss capability and magnetic-dielectric synergy. *J. Mater. Sci. Technol.* **2023**, *147*, 37-46. DOI
39. Deng, X.; Gao, S.; Yan, J.; et al. The green synthesis and enhanced microwave absorption performance of core-shell structured multicomponent alloy/carbon nanocomposites derived from the metal-sericin complexation. *J. Alloys. Compd.* **2021**, *882*, 160680. DOI
40. Hu, Y. P.; Zhou, T.; Zhang, D. H.; et al. Constructing ternary core-shell structured MWCNTs@Co/C@PANI nanocomposite for microwave absorption. *Rare. Met.* **2025**, *44*, 10594-606. DOI
41. Zhou, Z.; Zhu, Q.; Liu, Y.; Zhang, Y.; Jia, Z.; Wu, G. Construction of self-assembly based tunable absorber: lightweight, hydrophobic and self-cleaning properties. *Nano-Micro. Lett.* **2023**, *15*, 137. DOI PubMed PMC
42. Lv, Y.; Tian, J.; Chen, Z.; et al. MXene/bimetallic CoNi-MOF derived magnetic-dielectric balanced composites with multiple heterogeneous interfaces for excellent microwave absorption. *Chem. Eng. J.* **2023**, *478*, 147413. DOI
43. Wu, R.; Sun, Y.; Jiang, X.; Li, S.; Guo, S.; Yu, H. Hierarchical multi-shell hollow porous NiO/Co_3O_4 nanospheres with enhanced dielectric-magnetic synergy for high-efficiency microwave absorption. *Chem. Eng. J.* **2025**, *520*, 166063. DOI
44. Lan, X.; Wang, R.; Liu, W.; Huang, Z.; Deng, P.; Wang, Z. Multicomponent synergistic flower-like FeS/hollow C fiber for tunable and efficient microwave absorption. *Chem. Eng. J.* **2024**, *485*, 149238. DOI
45. Zhang, Y.; Pan, L.; Zhang, P.; Sun, Z. Gradient Multilayer Design of $Ti_3C_2T_x$ MXene nanocomposite for strong and broadband microwave absorption. *Small. Sci.* **2022**, *2*, 2200018. DOI PubMed PMC
46. Zhao, Q.; Li, F.; Liu, J. Analytical modeling of wave absorption performance in gradient graphene/polymer nanocomposites. *Materials* **2024**, *17*, 2946. DOI PubMed PMC
47. Wang, L.; Huang, M.; Yu, X.; et al. MOF-derived $Ni_{1-x}Co_x$@Carbon with tunable nano-microstructure as lightweight and highly efficient electromagnetic wave absorber. *Nano-Micro. Lett.* **2020**, *12*, 150. DOI PubMed PMC
48. Zhang, X.; Yan, F.; Zhang, S.; et al. Hollow N-doped carbon polyhedron containing CoNi Alloy nanoparticles embedded within few-layer N-doped graphene as high-performance electromagnetic wave absorbing material. *ACS. Appl. Mater. Interfaces.* **2018**, *10*, 24920-9. DOI PubMed
49. Wang, X.; Liu, J.; Han, X.; et al. One-dimensional multicomponent nanofibers engineered as heterostructures for electromagnetic stealth applications. *J. Alloys. Compd.* **2025**, *1028*, 180631. DOI
50. Li, Z.; Liang, J.; Wei, Z.; et al. Lightweight foam-like nitrogen-doped carbon nanotube complex achieving highly efficient electromagnetic wave absorption. *J. Mater. Sci. Technol.* **2024**, *168*, 114-23. DOI
51. Yu, J.; Luo, H.; Lv, S.; et al. Facile fabrication of melamine/MXene/FeNi-PBA composite derived multi-interface magnetic carbon foam for high-efficiency microwave absorption. *Adv. Elect. Mater.* **2024**, *11*, 2400265. DOI
52. Zare-nazari, F.; Dehghani-dashtabi, M.; Mohebbi, M.; Hekmatara, H. FeCu/MWCNT nanocomposite with a broad microwave absorption band and highly reduced radar cross section and farfield. *Adv. Elect. Mater.* **2025**, *11*, e00965. DOI
53. Ling, W.; Liao, P.; Zhu, J.; et al. Yolk-dual shell structured dielectric-magnetic SiO_2@C@void@$Ni_3ZnC_{0.7}$/C microspheres for boosting microwave absorption. *Chem. Eng. J.* **2025**, *520*, 166331. DOI
54. Shi, M.; Jia, Z.; Lan, D.; Gao, Z.; Zhang, S.; Wu, G. Enhanced polarization relaxation of multidimensional bimetallic selenide nanocomposites for electromagnetic wave absorption. *Adv. Funct. Mater.* **2025**, *35*, e02261. DOI
55. Shen, Y.; Ma, Z.; Yan, F.; Zhu, C.; Zhang, X.; Chen, Y. Enhanced interfacial polarization loss of FeS/MoS_2@N-doped carbon sandwich-walled nanotubes enables high-performance electromagnetic wave absorption. *Adv. Funct. Mater.* **2025**, *35*, 2423947. DOI

56. Xu, W.; Wang, S.; Xu, Y. Preparation of NiCo/NPC composites and study on their wave absorbing properties. *J. Mater. Sci.* **2024**, *59*, 3436-50. DOI

57. Liu, Y.; Zhou, J.; Li, C.; et al. Interfacial coupling effects in two-dimensional ordered arrays for microwave attenuation. *Nat. Commun.* **2025**, *16*, 202. DOI PubMed PMC

58. Lin, J.; Wen, H.; Feng, Z.; et al. Anion injection in dielectric ecosystems to construct dual built-in electric fields for efficient electromagnetic response. *Adv. Funct. Mater.* **2025**, *35*, 2505381. DOI